

Cavitation-induced microjets tuned by channels with alternating wettability patterns


Cite as: Phys. Fluids **35**, 032017 (2023); <https://doi.org/10.1063/5.0143223>

Submitted: 20 January 2023 • Accepted: 28 February 2023 • Accepted Manuscript Online: 02 March 2023
• Published Online: 21 March 2023

 Jelle J. Schoppink,  Keerthana Mohan, Miguel A. Quetzeri-Santiago, et al.

COLLECTIONS

Note: This paper is part of the special topic, Cavitation.

 This paper was selected as Featured



View Online



Export Citation



CrossMark

ARTICLES YOU MAY BE INTERESTED IN

[Drop impact on a sessile soap bubble](#)

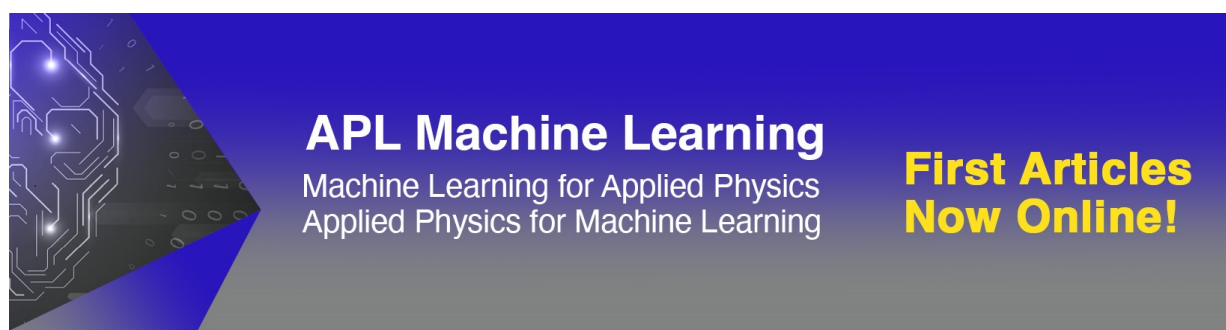
Physics of Fluids **34**, 122116 (2022); <https://doi.org/10.1063/5.0129427>

[Investigation of cavitation bubble dynamics near a solid wall by high-resolution numerical simulation](#)

Physics of Fluids **35**, 016115 (2023); <https://doi.org/10.1063/5.0135924>

[Effect of surface roughness and blade material on the performance of a stationary Savonius wind turbine under different operating conditions](#)

Physics of Fluids **35**, 035133 (2023); <https://doi.org/10.1063/5.0141119>



APL Machine Learning

Machine Learning for Applied Physics
Applied Physics for Machine Learning

**First Articles
Now Online!**

Cavitation-induced microjets tuned by channels with alternating wettability patterns

Cite as: Phys. Fluids **35**, 032017 (2023); doi: [10.1063/5.0143223](https://doi.org/10.1063/5.0143223)

Submitted: 20 January 2023 · Accepted: 28 February 2023 ·

Published Online: 21 March 2023



View Online



Export Citation



CrossMark

Jelle J. Schoppink,¹  Keerthana Mohan,¹  Miguel A. Quetzeri-Santiago,¹ Gareth McKinley,² 
David Fernandez Rivas,^{1,2}  and Andrew K. Dickerson^{3,a)} 

AFFILIATIONS

¹Mesoscale Chemical Systems Group, University of Twente, Enschede, The Netherlands

²Mechanical Engineering, Massachusetts Institute of Technology, Cambridge, Massachusetts 02139, USA

³Mechanical, Aerospace, and Biomedical Engineering, University of Tennessee, Knoxville, Tennessee 37996, USA

Note: This paper is part of the special topic, Cavitation.

^{a)}Author to whom correspondence should be addressed: ad@utk.edu

ABSTRACT

A laser pulse focused near the closed end of a glass capillary partially filled with water creates a vapor bubble and an associated pressure wave. The pressure wave travels through the liquid toward the meniscus where it is reflected, creating a fast, focused microjet. In this study, we selectively coat the hydrophilic glass capillaries with hydrophobic strips along the capillary. The result after filling the capillary is a static meniscus which has a curvature markedly different than an unmodified capillary. This tilting asymmetry in the static meniscus alters the trajectory of the ensuing jets. The hydrophobic strips also influence the advancing contact line and receding contact line as the vapor bubble expands and collapses. We present thirteen different permutations of this system which includes three geometries and four coating schemes. The combination of geometry and coatings influences the jet breakup, the resulting drop size distribution, the trajectory of the jet tip, and the consistency of jet characteristics across trials. The inclusion of hydrophobic strips promotes jetting in line with the channel axis, with the most effective arrangement dependent on channel size.

Published under an exclusive license by AIP Publishing. <https://doi.org/10.1063/5.0143223>

I. INTRODUCTION

The stability of liquid jets has captivated fluid mechanics for nearly two centuries,^{1,2} owing to both their mathematical complexity^{3–8} and usefulness.^{9–11} Recently, jet dynamics have gained attention from the engineering and medical communities for their use in drug delivery,^{10,12,13} ink-jet printers,^{14,15} and micro-fabrication.^{16,17} Such microscale jets rely on the sudden acceleration of a liquid column,^{18,19} piezoelectric actuation²⁰ or by rapidly vaporizing a portion of liquid upstream with a laser pulse (thermocavitation).^{21–24} Impulsively created jets are unsteady and are “kinematically focused” by a curved meniscus in which a pressure wave is reflected at the free surface.²² The focused liquid converges toward the center of curvature, resulting in jets with velocities that can exceed a Mach number^{22,25} $M = U/c_s = 1$, where U is the jet velocity and c_s is the speed of sound in air. Jets emerge from the focused menisci in the form of a stretched ligament that breaks into droplets. Numerous theoretical and experimental investigations have been carried out to explain the disintegration of liquid jets, which are inherently unstable.⁵ Various forces act on the surface of jets leading to disturbances that are amplified when

carried downstream, ultimately leading to jet breakup by the Rayleigh–Plateau instability among others.^{5,26,27}

The number and trajectory of droplets after jet breakup are guided by the characteristics of the initial impulse, bubble retraction in the case of thermocavitation, meniscus shape,^{28,29} and contact line motion. When the jet leaves the nozzle, the no-slip boundary condition is relieved at the outer radial edge, leading to the creation of radial velocity components within the jet. This profile relaxation generates instabilities in the jet.³⁰ Therefore, the jet characteristics can be modulated by modifying the initial meniscus shape and the nature of contact line motion.

The orifice geometry is another variable influencing jet disintegration.^{31,32} For non-circular nozzles, the propagating jet expands along one radial axis, while contracting in the other in an oscillating manner, destabilizing the jet.³² This so-called axis switching has been modeled as a spring-mass system driven by the competition of surface tension and inertia.³³ Jets produced by non-circular nozzles break up into smaller droplets and have shorter breakup lengths than comparable circular nozzles.³² These chain-like oscillations in the jet are caused

by non-axisymmetric perturbations which are less unstable than Rayleigh–Plateau instabilities. Chain-like oscillations are non-linear in nature, and their frequency decreases with increasing amplitude.³⁴ In a typical jetting experiment, the Rayleigh–Plateau instability is superimposed on non-axisymmetric perturbations to cause jet breakup.³⁴

In this study, we use an infrared laser pulse to create a cavitation bubble at the closed end of a microscale liquid channel and film the expulsion of the jet from two perpendicular views, as shown in Fig. 1. Our experimental system is similar to that established by Oyarte Gálvez *et al.*²¹ and earlier by Tagawa *et al.*,²² but here, we probe how the channel geometry and its wettability influence the jet characteristics. Two fundamental channel shapes are etched into borosilicate chips for experimental investigation, circular (C) and rounded rectangular (R) cross-sections, as shown in Fig. 2(a). The full length and relative height of each tested geometry, and the variety of jets they produce, are shown in Figs. 2(b)–2(d). Channel surface chemistry is either homogeneous (A1) or has alternating hydrophobic–hydrophilic sections (A2–A8) as depicted in Fig. 2(a). Due to manufacturing limitations, circular cross-sections have only three coating permutations, whereas rounded rectangles have five, for a total of thirteen unique channel configurations.

Our primary goal in this study is to unravel the connection between microchannel geometry and the subsequent jet properties. The jets created in these microfluidic channels are of interest for the role they may play in microscale liquid delivery devices. Such phenomena may be useful for applications such as the coating and spraying of surfaces, endoscopic procedures, and novel needle-free injections in the skin or the eye.²⁴ Though likely not sufficiently fast to break skin in a traditional approach,^{13,25,35} we employ more moderate jet velocities than our earlier work^{28,36,37} that allow for minimal damage of tissue and a higher spatiotemporal resolution.

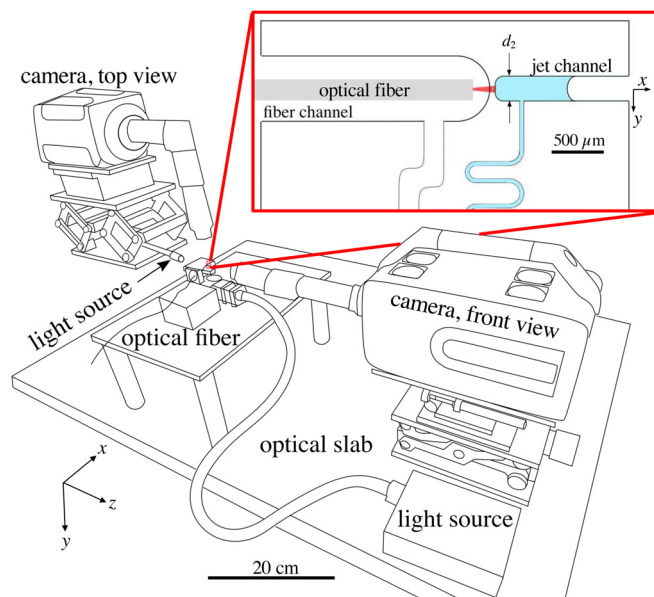


FIG. 1. Schematic of the experimental setup showing the orientation of the chip with respect to both camera views. The zoom box shows a glass chip in detail. Jets emerge from chips to the right.

The fabrication methods, experimental protocols, and further details of chip design are given in Sec. II. We present experimental results and discussion of jet velocity, droplet characteristics, repeatability, and focusing in Sec. III. We conclude our work in Sec. IV.

II. EXPERIMENTAL METHODS

A. Chip layout and fabrication

The overall layout of our experimental microfluidic chips is shown in Fig. 1. The fiber channel is nearly cylindrical and measures $425\ \mu\text{m}$ tall, $400\ \mu\text{m}$ deep, and $2450\ \mu\text{m}$ long. A $400\ \mu\text{m}$ channel is included to serve as an inlet and flush the fiber channel after fabrication to remove contaminants. All jet channels have a characteristic cross-section width $d_1 = 100\ \mu\text{m}$ and are $1850\ \mu\text{m}$ in length. Rounded rectangles have two size configurations, R2 and R3, such that $d_2/d_1 = 2$ and 3 , respectively. Relative channel size is shown in Fig. 2. The channel cross-sectional area A and perimeter P are computed using that of rectangles capped by two half-circles. Channel area A and hydraulic diameter $D_H = 4A/P$ are reported in Table I. Homogeneous glass channels (A1) are modified by selectively depositing atomically thin layers of gold that are thereafter soaked in thiol. The result is that channels have alternating sections of hydrophilic glass, $\theta_e \approx 30^\circ$, and hydrophobic gold, $\theta_e \approx 115^\circ$, where θ_e is the equilibrium contact angle. The arc length of coated and uncoated sections ℓ_1 , ℓ_2 , and ℓ_3 is shown schematically in Fig. 2(a) and provided in Table I. We henceforth refer to channels by an abbreviated identifier. For example, a rounded rectangle with a cross-sectional aspect ratio of three and six discrete alternating sections is referred to by R3A6. The jet channel is filled by a $360\text{-}\mu\text{m}$ glass capillary with distilled water, as shown in Fig. 1. The circular fill channel is $100\ \mu\text{m}$ in diameter and meanders to provide greater hydraulic resistance such that flow is preferential down the jet channel rather than toward the filling channel. Each gold strip begins $100\ \mu\text{m}$ from the closed end of the jet channel, as shown in Fig. 2(c).

Glass chips are fabricated under cleanroom conditions. The channel structures with half depths of 50 and $200\ \mu\text{m}$ are wet etched into 4-in. borosilicate glass wafers with a thickness of $500\ \mu\text{m}$. Next, a new photoresist is applied to the glass wafers and removed from the intended position of the gold structures. A $15\ \text{nm}$ thick coating of tantalum is applied prior to a $45\ \text{nm}$ thick coating of gold. The photoresist is removed, and a gold layer remains only on the intended positions. Afterward, two glass wafers are bonded together and diced to create single chips. The gold surface is made hydrophobic according to Notsu *et al.*³⁸ The chips are immersed for $1\ \text{h}$ into a $10\ \text{mM}$ solution of 1H, 1H, 2H, 2H-perfluorodecanethiol (PFDT, Sigma Aldrich) in ethanol, after which the channels are flushed with ethanol to remove any excess PFDT. The PFDT has no effect on the borosilicate glass.

B. Jet creation and high-speed imaging

Jets are created by the vaporization of water on the closed end of jetting channels by a $10\ \text{ms}$, $1.95\ \mu\text{m}$ infrared laser pulse with a power of $0.59 \pm 0.03\ \text{W}$. Due to the high-absorption coefficient of water at this wavelength ($\alpha \approx 120\ \text{cm}^{-1}$) (Ref. 39), no dye is required, in contrast to our previous work.^{21,28,40} The channels are filled to approximately $925\ \mu\text{m}$ from the surface where the laser light enters the liquid, much greater than the $\approx 80\ \mu\text{m}$ absorption length.

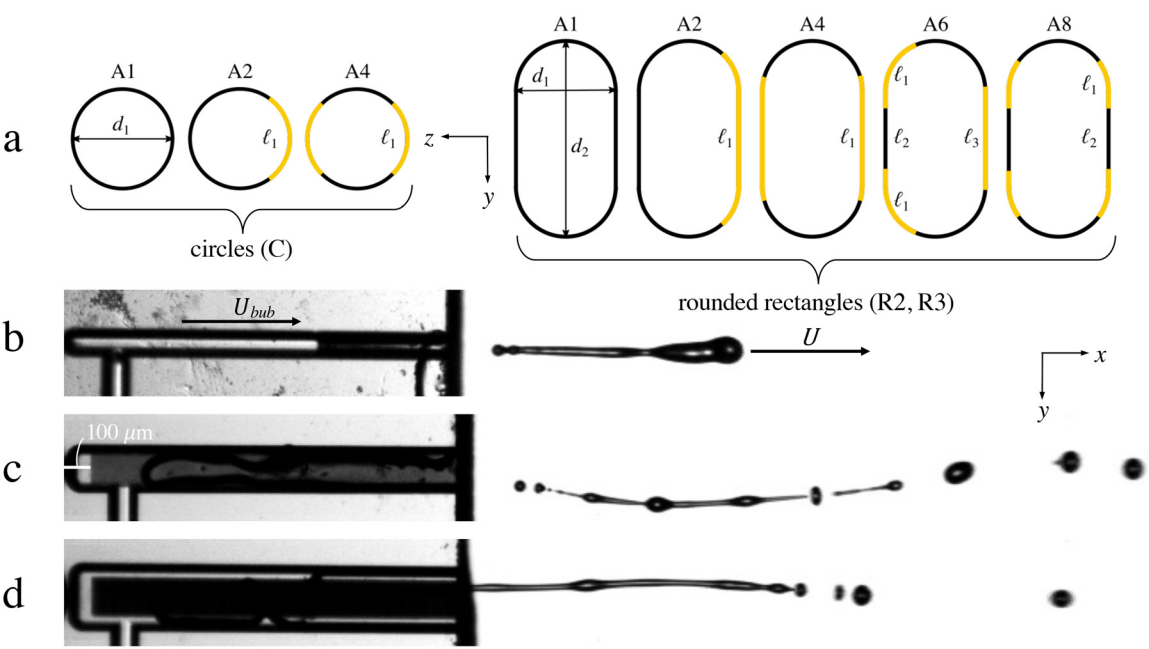


FIG. 2. (a) Schematic of channel inner surface coating and cross-section permutations, and representative jet images from channels. Diagrams are such that the camera views them looking from left to right. (b) CA1, (c) R2A2, and (d) R3A4. Every channel is 1850 μm long and 100 μm deep into the frame. Other pertinent dimensions are given in Table I.

TABLE I. Channel and coating parameters.

Geometric configuration Coating configuration	C			R2					R3				
	A1	A2	A4	A1	A2	A4	A6	A8	A1	A2	A4	A6	A8
d_1 (μm)	100
d_2 (μm)	200	300
ℓ_1 (μm)	...	103	84	...	193	128	77	64	...	293	178	97	89
ℓ_2 (μm)	64	64	98	89
ℓ_3 (μm)	107	107	...
A (μm^2)	...	7854	17 854	27 854
D_H (μm)	...	100	139	156

All the non-reflected energy is, thus, absorbed by the water and we assume that reflected light is negligible and constant across all chips. The laser pulse is produced by a Thulium fiber laser (BKTel Photonics) with an SMF28 optical fiber output. The fiber is cleaved prior to use and the fiber tip is placed at a distance of 250 μm from the closed end of the jet channel. The laser power has a secondary fiber output of 1% of the nominal power, which is monitored by a photodetector (Thorlabs DET05D2). To confirm the actual laser power, the photodetector is read out by an oscilloscope (Tektronix MSO 2014B). The absorption coefficient in distilled water at the wavelength of the laser (1950 nm) is approximately 120 cm, and so, the length over which laser energy is absorbed by the water is approximately 80 μm .

Jetting events are filmed at two perpendicular angles by a Photron SA-X2 (Front view, x, y) and a Photron Nova S6 (Top view, x, z) at 144 000 fps. Both cameras are equipped with a Navitar 12 \times zoom lens, operating at magnifications of 3 \times and 2 \times , respectively. Backlighting is provided by a Schott Coldvision-LS and SugarCUBE Ultra. All equipment is triggered simultaneously by an Arduino UNO. Only select channel configurations were imaged from the top view. Priority was given to the asymmetrically coated channels. Therefore, the non-coated (CA1, R2A1, R3A1) and some symmetrically coated (R2A4, R2A8) are only imaged from the front. For the other eight chips, the jet was imaged from the front and top simultaneously. Videos were processed by custom code in MATLAB that binarized images to measure droplet size and position. Binarization is done with MATLAB's imbinarize

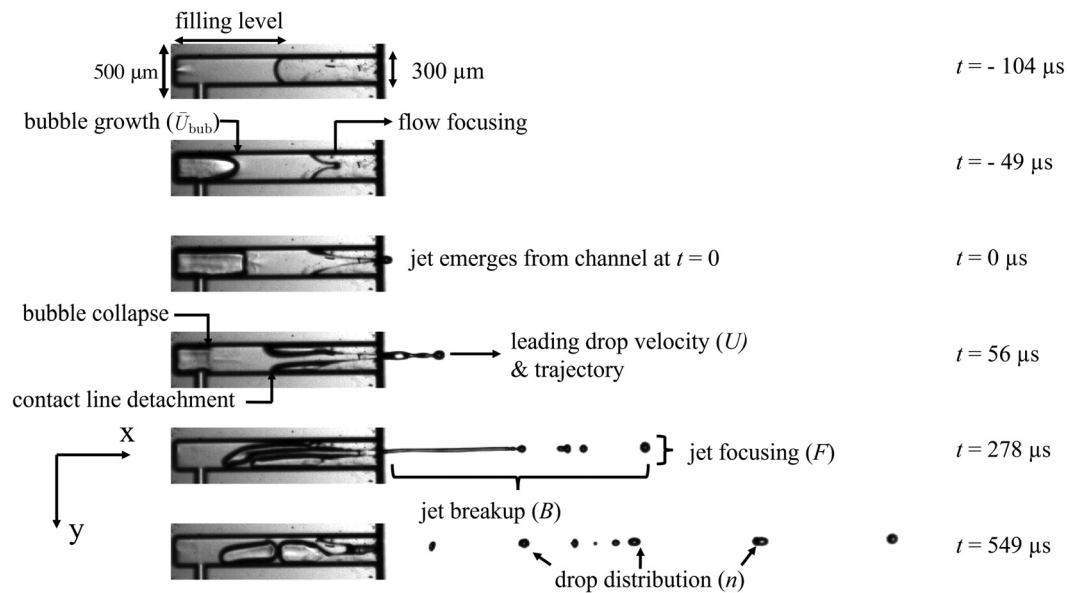


FIG. 3. Sequence of images showing the jetting event. Each element of the complete jetting event will be discussed in a specific subsection: Bubble growth and initial jet formation, etc.

function with no dilation or erosion imposed. To reduce binarization noise, we filter isolated groups of pixels, including the smallest droplets, less than $20\ \mu\text{m}$ or 3 pixels in diameter.

III. RESULTS AND DISCUSSION

We filmed approximately twenty jetting events from each thirteen channel configurations. The inclusion of PFDT-bonded gold coating in ten of the thirteen channels results in channels with a heterogeneous wetting condition. A typical jetting event is depicted in Fig. 3, where all the stages of the process are signaled. Channels are filled to half their length, $\sim 850\ \mu\text{m}$, before activation of the laser pulse. Prior to bubble formation, a spot of non-homogeneous light intensity appears near the laser spot position, which we posit is due to an augmented refractive index caused by localized heating. Expansion of the laser-induced bubble drives the kinematically focused meniscus forward. We set $t = 0$ at the moment the jet emerges from the channel. A half-fill in our channels is done deliberately such that all moving menisci are allowed an equal and substantial runway length along the coated or uncoated channel walls. Channels that are fully filled do not experience the same degree of meniscus focusing and are only affected

weakly by channel coating as the jet tip exits the channel, likely the result of not having a statically curved meniscus.²⁸ An example of CA1 fully filled is provided in Fig. 4 (Multimedia view). Jets from completely filled channels tend to be larger in diameter, with a thicker tip.²⁸ In the case of Fig. 4, the large tip flattens against air resistance as it emerges. On the other extreme, channels not sufficiently filled experience the breakup of the liquid plug before the jet exits, a phenomenon more likely as channel cross-sections grow in the area from chip to chip.

The sheer amount of data produced in this study precludes a full presentation of our results below, and we, thus, select six from the thirteen nozzles fabricated to feature in this main text. A comprehensive presentation of plots from all nozzle permutations is provided in the [supplementary material](#) (Figs. S1–S13). For each geometric configuration, we feature the uncoated (A1) and a coated configuration providing the lowest focusing factor F , which is to be described in Sec. III F. Our featured nozzles are denoted in red text in Table II.

A. Bubble size and jet velocity

Thermocavitation is a stochastic process, and there is an energy barrier that must be crossed to generate the bubble inside the channel.



FIG. 4. The jetting sequence of a fully filled CA1 channel. The panels show the moments of jet emergence from the channel (top), maximum bubble size (middle), and complete bubble collapse. Multimedia view: <https://doi.org/10.1063/5.0143223.1>

TABLE II. Jet characterization parameters. Featured channels are highlighted in red. N indicates the number of videos. U/\bar{U}_{bub} indicates the slope of the linear fit of $U(\bar{U}_{\text{bub}})$, and R^2 , $U \sim \bar{U}_{\text{bub}}$ indicates the R^2 -value representing the quality of this fit. B^* indicates the breakup factor, F the focusing factor.

Geometric configuration Coating configuration	C			R2					R3				
	A1	A2	A4	A1	A2	A4	A6	A8	A1	A2	A4	A6	A8
N	21	20	20	20	20	20	42	20	20	22	20	20	21
U/\bar{U}_{bub}	0.87	0.58	0.68	0.83	0.75	0.80	0.81	0.85	0.90	1.52	1.29	1.07	1.16
R^2 , $U \sim \bar{U}_{\text{bub}}$	0.84	0.79	0.75	0.95	0.73	0.94	0.92	0.90	0.91	0.43	0.70	0.27	0.35
Re	2000	1409	1325	1812	1323	2105	1545	1660	1967	892	1501	1210	1352
	± 303	± 234	± 359	± 238	± 144	± 412	± 301	± 234	± 347	± 596	± 465	± 259	± 344
We	444	221	204	261	138	359	172	219	278	79	171	106	135
	± 134	± 71	± 116	± 67	± 29	± 148	± 69	± 64	± 99	± 70	± 124	± 41	± 52
\bar{T} (μs)	263	358	432	365	370	334	458	427	408	484	521	563	491
	± 43	± 102	± 121	± 170	± 162	± 89	± 180	± 157	± 167	± 266	± 184	± 196	± 178
B^* ($\tau = 1/3$ ms)	0.81	0.71	0.75	0.89	0.91	0.89	0.87	0.89	0.87	0.84	0.64	0.85	0.84
F (μm)	138.9	92.6	92.1	238.2	195.2	103.8	121.4	111.6	161.1	208.4	82.2	69.3	124.2

In some cases, the bubble forms early when the amount of absorbed energy is still low, generating a relatively small bubble. In others, the bubble forms later when the amount of absorbed energy is greater, forming a larger bubble. Zhang *et al.*⁴¹ report a variation bubble size of approximately 50%, even for experiments with identical initial conditions.

The maximum bubble size, bubble expansion velocity, and filling level all influence jetting from a given channel geometry. Small bubbles (less than 20% of channel length) create jets with little volume, often a few discrete droplets (of diameter 50 μm), Fig. 5 (Multimedia view). However, all jets presented here are well above the transition from dripping to jetting,⁴² given by a velocity at or less than 2.5 m/s. By contrast, larger bubbles produce a more complete emptying of the channel

often with a curved jet tail (which we refer to as tail sway), see Fig. 6 (Multimedia view). Bubbles with sizes comparable to the channel length can empty the channel almost completely, and the jet exits as a plug. The jet tip, in this case, is also thicker similar to that of a fully filled channel. There exists an optimum range of bubble sizes vs filling levels for a given channel geometry in which a jet can be produced without the extreme cases of droplet or plug formation. For example, in the R2 channels, the transition to plug flow was observed for bubbles between 1.1 and 1.4 times the initial filling level, but its precise definition will be the topic of future work.

The relation between jet velocity (U) and the average velocity of the bubble front during its growth phase (\bar{U}_{bub}) is plotted in Fig. 7.

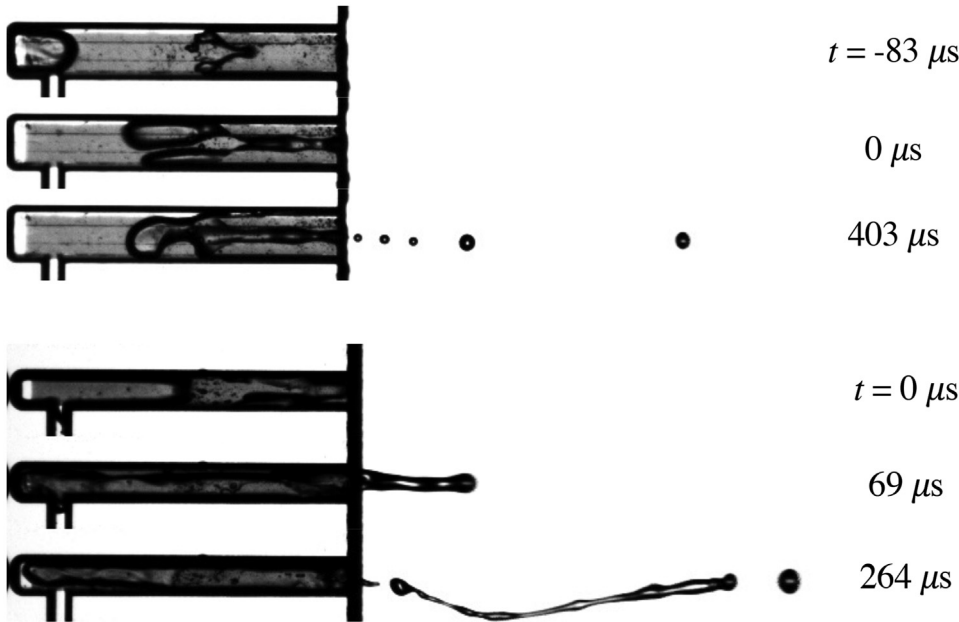


FIG. 5. The jetting sequence produced by a relatively small bubble, less than 20% of the channel length. The panels show the moments of maximum bubble size (top), jet emerge from the channel (middle), and when the last droplet breaks from the main jet body within the channel (bottom). Multimedia view: <https://doi.org/10.1063/5.0143223.2>

FIG. 6. The jetting sequence produced by a relatively large bubble, resulting in a swaying jet tail. The panels show the moments of jet emergence (top), complete bubble collapse (middle), and when the final droplet breaks from the main jet body within the channel (bottom). Multimedia view: <https://doi.org/10.1063/5.0143223.3>

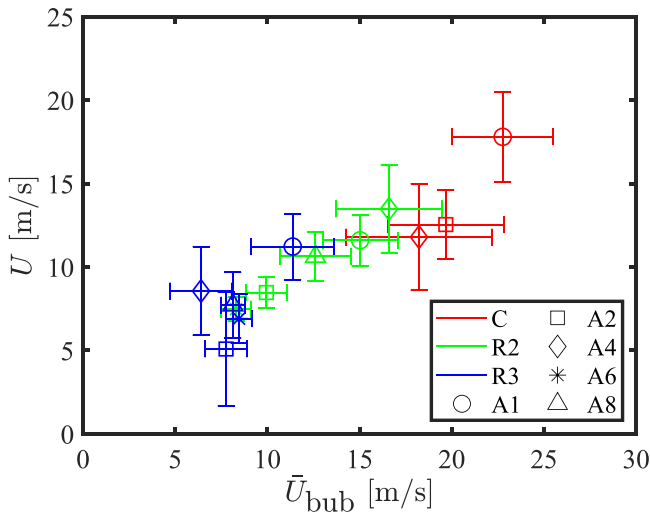


FIG. 7. Jet velocity vs average bubble velocity for all channels. For the circular channels, the hydrophobic coatings lower U/\bar{U}_{bub} compared to uncoated channels. For R2, the effect of the coatings is negligible. In the case of larger R3 channels, coatings increase U/\bar{U}_{bub} compared to uncoated channels. Values of U/\bar{U}_{bub} provided in Table II.

We determine the jet velocity by tracking the leading edge of the jet tip from the moment it exits the chip at $t = 0$ for ten frames ($69.4 \mu\text{s}$). For all configurations, U/\bar{U}_{bub} and correlation coefficients for $U = j\bar{U}_{\text{bub}}$ are given in Table II, where j is a fitting constant. We here note the first distinction between jets from circular (C) and rectangular (R) channels. The relatively small circular channels experience the fastest bubble expansion, producing the fastest jets. Both coated circular channels exhibit a lower aggregate U and U/\bar{U}_{bub} when compared to CA1. In rectangular channel R3, coatings increase U/\bar{U}_{bub} over the uncoated configuration.

We use jet velocity U and hydraulic diameter D_H to define other common dimensionless groups used in jetting studies: Reynolds number $Re = \rho U D_H / \mu$, Weber number $We = \rho U^2 D_H / \sigma$, and Ohnesorge number $Oh = We / Re^2$. Here, the density, viscosity, and surface tension of distilled water are taken to be $\rho = 1 \text{ g/mL}$, $\mu = 0.89 \text{ cP}$, and $\sigma = 72.9 \text{ dyne/cm}$, respectively. We report average Re and We for all channels in Table II. The range of Reynolds number, 175–3125, indicates inertia dominates viscosity in our jets. We note, however, that flow focusing on the meniscus creates jets that have a characteristic size $\sim 1/3$ the diameter of the rectangular (R) channels. A reduction of our calculated Reynolds numbers by a factor of three does little to stifle the apparent inertia dominance. Our experimental range in Weber number, 2–664, indicates that for our slowest jets, surface tension plays a large role in their behavior. The slowest jets arise from R3 channels and experience rapid ligament disintegration into droplets. It is of no surprise from the dominance of inertia and surface tension that the Ohnesorge number is low for all channels. The Ohnesorge number $Oh = 0.0104, 0.0088$, and 0.0083 for (C), (R2), and (R3), respectively.

B. Jet breakup and the breakup factor

For a quantitative measure of how coherent jets break into drops throughout the jetting event, we define the “breakup factor” B .

The breakup factor is a ratio of the total liquid parcel length along the jetting axis to the distance between the tip of the leading drop to the tail of the trailing drop. To make B comparable across different channels, we define the *primary jetting event* from the moment the jet tip leaves the chip at $t = 0$ to the moment the leading drop leaves the frame at $t = T$. The average value of T for each channel \bar{T} across N trials is reported in Table II. Most often, jets exit the field of view (FOV) at the rightmost edge (approximately $4850 \mu\text{m}$ from the channel exit) but may exit earlier through the top or bottom of the FOV. An example of the window taken to measure B is shown by the bounding red lines in the top panel of Fig. 8. Mathematically, the breakup factor is represented by

$$B(t) = \frac{1}{(x(t)_{c,1} + D_1/2) - (x(t)_{c,n} - D_n/2)} \sum_{i=1}^n D_i, \quad (1)$$

where n is the number of liquid parcels (either drops or ligaments) in the observation window, D_i is the equivalent diameter of the i th liquid parcel, and x_c is the lateral centroid location of a liquid parcel. The denominator of Eq. (1) is the width of the window over which the breakup factor is measured. A nozzle emitting a single drop, or an unbroken column of liquid, has a breakup factor of unity for all time. We average the breakup factor across N videos and plot \bar{B} vs jetting time t in Fig. 8 for our featured channels. Since each individual jet leaves the frame at a different time, the number of trials used to calculate the \bar{B} curve reduces as time progresses. The blue curves represent the fraction of trials N that contribute to $\bar{B}(t)$. The red “x” on the vertical axes represents the fraction of videos in which the leading drop exits the frame on the right, rather than the top or bottom. The area under the $\bar{B}(t)$ curve can be compared to an unbroken jet that maintains $B = 1$ for some specified time τ . Accordingly, we define this ratio as

$$B^* = \frac{1}{\tau} \int_0^\tau \bar{B} dt. \quad (2)$$

We set $\tau = 1/3 \text{ ms}$ such that we can compare B^* values across all channel configurations; after this time, \bar{B} is undefined for some channels because all their respective leading drops have reached the boundary of the FOV. We report the values of B^* in the plots of Fig. 8 and Table II. The choice of τ plays a large role in the value of B^* . At short times (up to $\tau \approx 0.1 \text{ ms}$), B^* tends toward unity, while for the circular channels $B^*(0.5 \text{ ms}) = 0.55 \pm 0.02$ except for CA1 where $B^*(0.5 \text{ ms})$ is not defined. Similarly, for the rectangular channels $B^*(0.5 \text{ ms}) = 0.72 \pm 0.02$ except for R2A4 for which $B^*(0.5 \text{ ms})$ is not defined and R3A4 for which $B^*(0.5 \text{ ms}) = 0.51$. In other words, B^* decreased $\approx 25\% \pm 5\%$ from $\tau = 1/3$ to $\tau = 1/2 \text{ ms}$. Of our featured channels, R3A6 retains the most videos through time of any channel but has the lowest average jet velocity, a likely contributor to its propensity for producing axially focused jet trajectories. From the values of B^* , we find that hydrophobic coatings do not promote or delay breakup in comparison to homogeneous channels.

C. Droplet size distribution

The distribution of equivalent drop diameter at the end frame of the primary jetting event, $t = T$, is shown for featured nozzles in Fig. 9. Bin sizes are $20 \mu\text{m}$, starting at $20 \mu\text{m}$. Below $20 \mu\text{m}$, drops are less than three pixels across and are filtered by our binarization algorithm. The majority of drops present at $t = T$ range from 40 to $60 \mu\text{m}$, a dominance that is generally enhanced by coating. The droplet

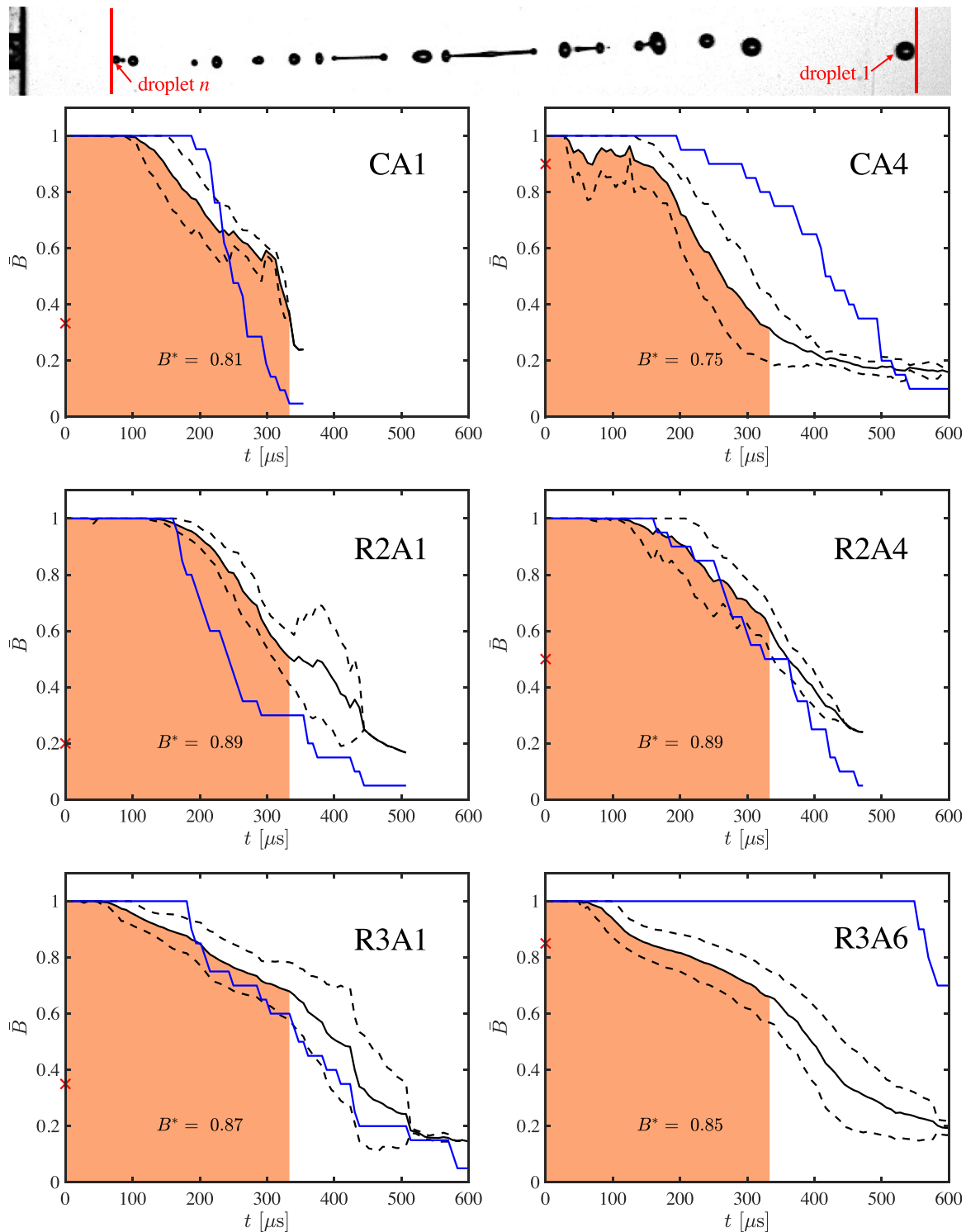


FIG. 8. Breakup factor vs jetting time for featured channel configurations. Dotted lines represent standard deviation bounds, which are limited to not exceed $B = 1$. Values printed beneath curves correspond to Eq. (2). Blue curves represent the fraction of trials contributing to $\bar{B}(t)$ and the red \times on the ordinates correspond to the number of trials in which leading drops leave the right-hand side of the FOV. Top panel: A representative photograph of jet breakup with red lines bounding the breakup window in Eq. (1). The jet, emitted from an R2A6 channel has $U = 8.64$ m/s, $Re = 1350$, $We = 142$, and $T = 583$ μ s.

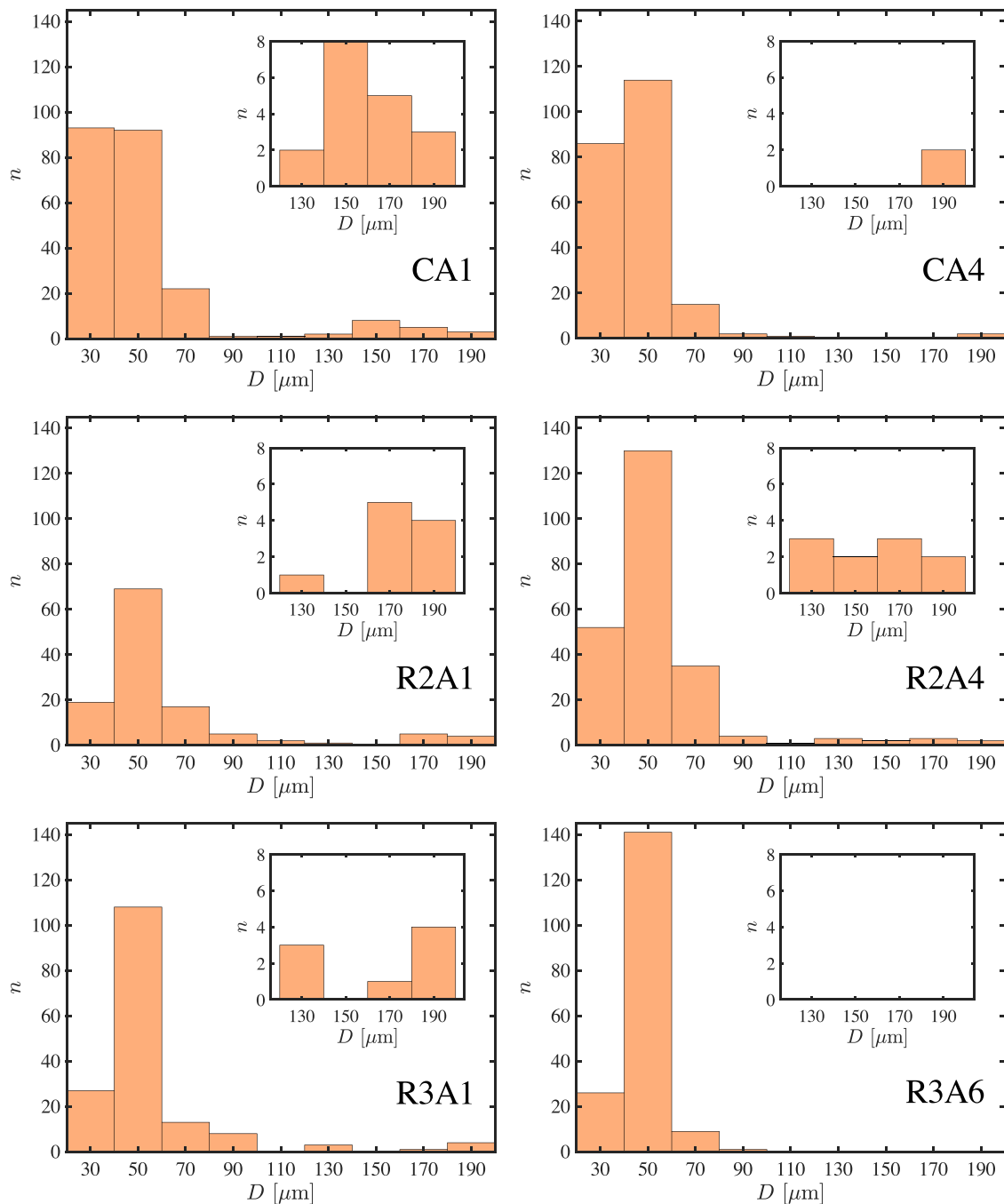


FIG. 9. Drop distribution histograms at $t = \bar{T}$ for featured nozzles. Histogram bin sizes are $20 \mu\text{m}$, and insets are zoomed views of bins $>120 \mu\text{m}$. \bar{T} is provided for all channels in Table II.

breakup in our system is highly dependent on multiple factors and varies even for jets ejected at similar conditions. This leads to a wide-size distribution that is typical for uncontrolled breakups.⁴³ For such random breakup processes that involve fragmentation and coalescence,^{43–45} previous works fit a gamma distribution to the drop size

histogram. Our attempt to do the same does not yield additional, useful information on the distribution of drops produced by our jets. We believe the lack of efficacy of the gamma distribution is a result of our relatively low droplet count compared to other spray studies and the stochastic nature of our jetting events.

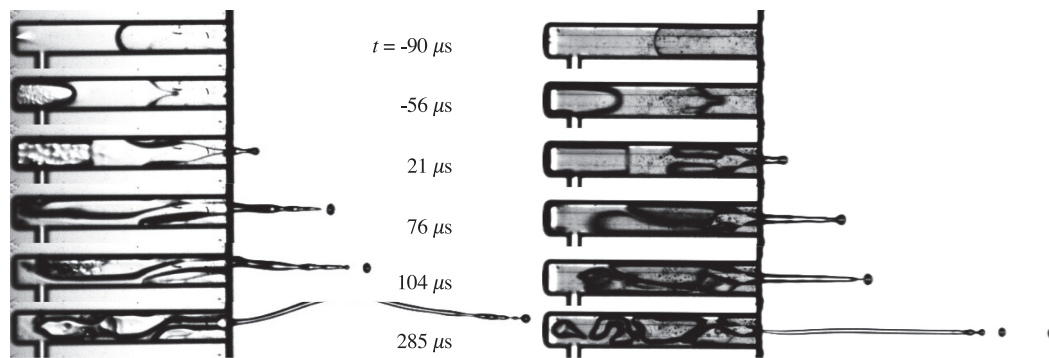


FIG. 10. Time sequences of bubble expansion and partial collapse for R3A1 (left, $T = 382 \mu\text{s}$, $U = 10.96 \text{ m/s}$, $Re = 1920$, $We = 257$) and R3A6 (right, $T = 500 \mu\text{s}$, $U = 8.36 \text{ m/s}$, $Re = 1470$, $We = 150$) at comparable time steps following nucleation ($t = 0$).

D. Jet trajectories

We find the shape of the static meniscus formed during channel filling to be the primary factor influencing the directional bias of jet tips. Symmetric static menisci wet the opposing walls equally to produce jet tips that exit the channel aligned with the channel centerline. Channels R3A1 and R3A6 pictured in Fig. 10 have a symmetric coating pattern when viewed from the front and, thus, when filled have a symmetric static menisci. From Fig. 10, the formation of self-focused jet tips is observed at $t = -56 \mu\text{s}$, and the exit of these focused tips from the channels is seen at $t > 0 \mu\text{s}$.

Asymmetrically coated channels form asymmetric static menisci that bias the jet tip trajectory. We present the average trajectory of the jet tip in Fig. 11. The variance in trajectories indicates that coatings, by way of the static menisci shape, influence the direction of the average leading drop. Average trajectories are calculated as follows: first, the individual jet tip trajectories are obtained from the videos. Then, for all x -values, the average is taken of all individual jet tips. In some cases, the jet tip leaves the FOV through the top or bottom edge ($y = \pm 250 \text{ m}$ or $z = \pm 320 \text{ m}$) instead of the rightmost edge (at $x = 4750 \text{ m}$). In this case, an individual trial does not contribute to the average trajectory plot for x -values larger than where it left the FOV. The shaded regions in Fig. 11 indicate the standard deviations from the average trajectory. Front view trajectories (x, y view) are available for all channels and are shown in orange. The trajectories of the top view (x, z), where available, are shown in blue.

1. Front view y trajectories

For all channels, including those with hydrophobic coatings, their static menisci are expected to be symmetric in the y direction due to the symmetry of the coatings in y . Gravitational forces in our system are negligible. Therefore, we do not expect any systematic directionality in the front view (Fig. 10). However, local surface defects can generate nonsystematic exceptions because they may cause an initial asymmetric static meniscus. The defects are usually microscopic imperfections on the glass or gold surfaces formed during fabrication. If the defects are present at the exact locations where a channel is filled, the asymmetric static meniscus that is subsequently formed can change jet trajectories. The presence of these defects and their significance can be discerned only by viewing jetting behavior after the

experimental trial. We find this to be the case for the trajectory deviations in R3A8 and R3A6. Otherwise, as expected, the deviation of the jet in the vertical y -direction from the centerline does not show a systematic bias, with the exception of CA1. The CA1 directionality can be attributed to the unintentional upward tilt of the chip in its holder.

2. Top view z trajectories

In contrast to the deviation in the y -direction, trajectories in z show a clear bias away from the channel centerline, especially the asymmetrically coated channels (A2 and A6). Trajectories bias toward the z -direction, or to the right-hand side in the channel schematics in Fig. 2(a). For the three symmetric channel configurations with top views (CA4, R3A4, R3A8), only R3A4 shows a small bias toward $-z$ (1.25). Therefore, we can conclude that the bias of the asymmetric channels is caused by coating asymmetry and not by camera or chip misalignment. For asymmetrically coated channels, the bias is toward the hydrophobic gold coating for A2 and toward the centered hydrophobic gold strip for A6. Of these two patterns, the A6 channels show a greater bias, and R3A6 exhibits the most extreme case of bias toward the z -direction. The extreme bias of R3A6 is lost in Fig. 11 because almost all the jet tips leave the FOV in the z -direction and most at $x < 3000 \mu\text{m}$, after which they no longer contribute to the average trajectory. Thereafter, the contributions of the jet tips closer to the centerline become more significant, and the average trajectory shifts back toward the centerline.

3. Contact line effects on jet trajectory

Here, we explain how the contact line dynamics and the wettability of the channels affect the meniscus focusing, the tip bias, and the tail movement out of axis. As discussed previously, for asymmetric channels, the jet tips and body trajectories have a bias toward the hydrophobic coating (see Figs. 11 and 16). Initially, this bias may seem counter-intuitive; however, the static meniscus shape holds the key. For asymmetrically coated channels, the contact line at the hydrophilic walls is further advanced down the channel axis compared to the hydrophobic channel wall, as depicted in Fig. 12. Therefore, the static meniscus is slightly tilted toward the z -direction, with its surface normal directed toward the hydrophobic wall. At the moment of jet formation, the tilted meniscus results in an off-axis jet. Thus, meniscus

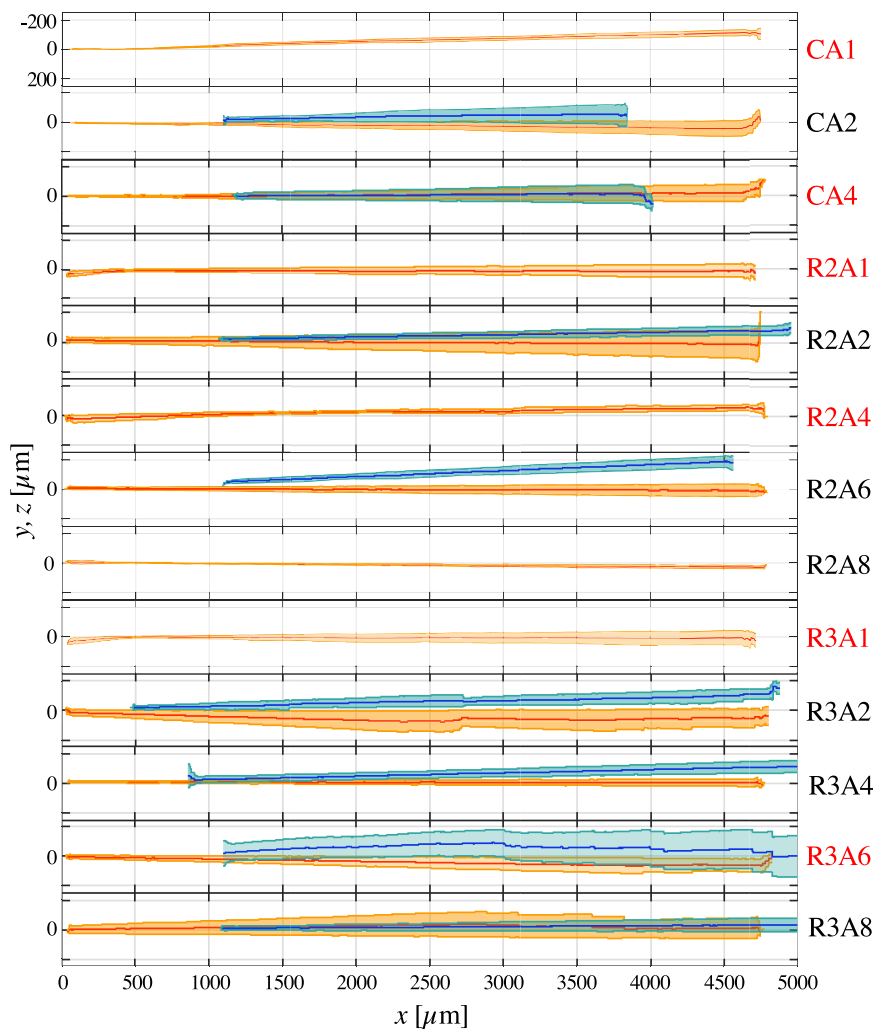


FIG. 11. Average trajectory of jet tips from front (red, y) and top (blue, z) views with standard deviation shaded regions in orange and light blue, respectively. The y , z -dimension for each panel is $\pm 250 \mu\text{m}$, with an inverted axis, such that negative y , z -values are up. Featured channels are labeled with red text. Coatings generate no systematic bias in y . Coating configurations which are asymmetric about the x - y plane bias jets toward $-z$ as seen from a top view.

shape dictates the tip direction and governs the initial stages of the jet ejection.

As the jet continues to exit the channel following the leading drop, liquid is expelled and the bubble begins to retract. The contact line on the jet side of the liquid remaining in the channel often detaches from the channel walls at different times and locations, a phenomenon we term “asymmetric contact line detachment,” which is shown for R3A1 in the image sequences of Fig. 10 (left) at $t = 21$ and $76 \mu\text{s}$. Asymmetric detachment creates a deviation in the jet body away from the trajectory set by the jet tip, exhibited by the R3A1 jet at $t = 104 \mu\text{s}$ in Fig. 10. The jet body shifts toward the upper channel wall, and at $285 \mu\text{s}$, the curved jet tail leaves the FOV. The sway does not affect the highly inertial jet tip, which continues on its course. Altogether, the jets that experience asymmetric contact line detachment have a large spread of intensities in the spatiotemporal diagrams (STD) in y and a low focusing factor F .

Asymmetric detachment has been observed to arise from: (i) the presence of $< 20 \mu\text{m}$ sized air bubbles present on the upper or lower

walls, introduced during channel filling. These bubbles burst during the rapid advancement of the contact line, contributing to detachment. (ii) Contact line hysteresis due to local surface defects originating from chip fabrication. (iii) A vertical eccentricity of approximately 20 – $30 \mu\text{m}$ in the location of bubble nucleation, resulting in asymmetric bubble expansion and, therefore, asymmetric contact-line detachment. The presence of hydrophobic coatings can help reduce the extent of the effects of asymmetric detachment on the jet body. An example of contact line detachment stabilization can be seen in Fig. 10 (right) for R3A6, where an asymmetric detachment at $t = 76 \mu\text{s}$ is not propagated to the jet body. The contrast in wetting between the hydrophilic and hydrophobic strips stabilizes the liquid bulk supplying the jet. This wetting contrast effectively creates energy barriers at the hydrophobic strips that maintain the liquid within the hydrophilic strip. Therefore, the jet body continues to exit from the liquid bulk centerline, as seen at $t = 104$ and $285 \mu\text{s}$.

For channel R3A8, in most cases, we observe that the jet body remains centered by adhering to the central hydrophilic strips.

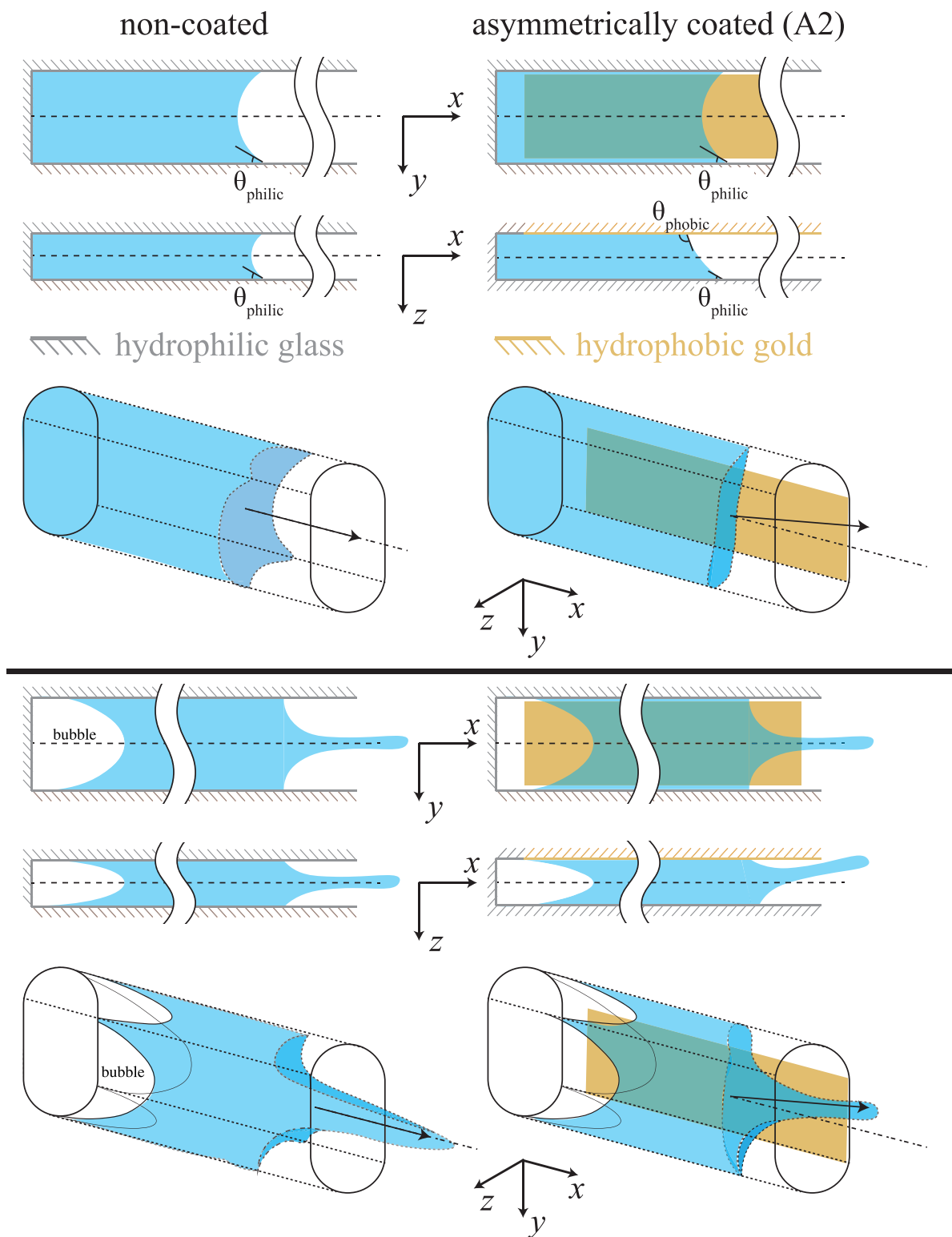


FIG. 12. Front (x, y), top (x, z), and isometric (x, y, z) schematics of the static meniscus (upper panels) and flow-focusing effect during bubble expansion (bottom panels). A non-coated channel is shown on the left column and a coated channel (A2) on the right.

However, in cases with an asymmetric static meniscus, the jet tip has a bias toward the top or bottom, for which reason the jet leaves the center strip and moves toward the hydrophilic strip in the top or bottom of the channel. This deviation can be explained due to the smaller size of the centered hydrophilic strip compared to the R3A6 (89 and 98 μm for R3A8 and R3A6, respectively), as well as the smaller extent of the hydrophobic strips surrounding the hydrophilic strip (89 and 97 μm , respectively). Therefore, the energy barrier for moving toward the top or bottom surfaces and wetting them is smaller, resulting in a larger fraction of the jets leaving the channel biased toward the top or bottom. For R3A4 and R3A2, the initial jet formation is centered. However, in the case of asymmetric liquid detachment, the tail of the jet sways. The sway occurs as there are no energy barriers, i.e., there is no hydrophilic strip that keeps the liquid in the center of the channel, in contrast to A6 and A8 channels.

Compared to R3 chips, the R2 chips experience a greater average bubble velocity \bar{U}_{bub} . In some cases, this larger average bubble velocity results in the formation of plug flow instead of a focused jet tip. Furthermore, the centered hydrophilic strip in R2A6 and R2A8 is smaller compared to their R3 counterparts. Therefore, the diameter of the plug is larger than the centered hydrophilic strip, resulting in the wetting of one or both hydrophobic strips. This means that the contact line is no longer contained between the interface of the hydrophilic–hydrophobic strips, and the energy barriers are overcome by the initial inertia of the system. Thus, the jets are not centered and can exit along the top or bottom of the channel. For the circular channels, due to their smaller cross-sectional area (less than half that of R2 channels), average bubble velocities are larger than for rectangular channels, resulting in plug flow in all cases. The jet diameter is of similar size to the channel (100 μm); therefore, the contact lines slide along the channel walls to the channel exit. Because the initial cavitation bubble is of the same size as the channel length, all liquid is expelled and there is no receding contact line. Therefore, there is little sway of the jet body and tail.

E. Spatiotemporal diagrams in x

The jets produced from our system behave like a high-momentum fluid ligament, with pinch-off occurring as the jet travels forward.^{5,46} The liquid remaining in the channel acts as a “reservoir” that feeds the ligament with the expansion of the cavitation bubble. With the bubble collapse and the ejection of the remaining liquid, the ligament pinches off from the reservoir and breaks up into a string of droplets as shown in Figs. 2(c) and 2(d). A convenient way to visualize the dynamical behavior of this ligament is a spatiotemporal diagram (STD) or kymograph, which shows the evolution of the jets in a single space dimension and time. In the STDs, x is the coordinate parallel to the channel’s long axis, and t is the perpendicular coordinate. For convenience, the edge of the channel (or nozzle) from which the liquid emerges is set as $x = 0$; the time at which this occurs corresponds to $t = 0$. In the STDs, therefore, we visualize the jet as it emerges from the nozzle and travels in time through the field of view (FOV) to the right of the nozzle.

STDs are created from the binarized video frames of a jetting event. Every binarized frame consists of the liquid (ligament or drops) in white against a black background. An STD created for a single video is shown adjacent to representative frames in Fig. 13 (top). For the STD in x , the binary matrix for a frame is summed along each column, resulting in a row vector with a range of “intensities.” Row vectors for

each frame are stacked onto one another to form the STD in x , which is an $i \times j$ matrix, where i is the number of frames and j is the number of x -pixels in the FOV. Liquid parcels which are longer in the direction of travel create a larger footprint in x (spanning more pixels). Long unbroken lengths generally indicate ligaments, while individual lines indicate the motion of droplets. The height normal to the jetting axis (in y) of a liquid parcel, drop or ligament, for a single frame is represented by intensity values. Breakup is indicated by the splitting of a line and the velocity of a liquid parcel is given by the inverse of the slope of its line in the STD. Aggregated STDs in x are shown for our featured channels in Fig. 13 (bottom) which show the average axial behavior of the channel. Aggregates are formed by combining individual STDs for every trial (usually 20) for a given channel. Individual STDs are truncated to the shortest captured video in time and averaged by the number of videos (Table II) and then normalized by the maximum intensity to create the aggregated STDs for that channel configuration, see Fig. 13 (bottom). Therefore, all STDs in Fig. 13 (bottom) have an intensity range from 0 to 1.

In the aggregated STDs in Fig. 13, trajectories of individual drops remain distinguishable. The leading drops are found at the top surface of the wedge-like spray emanating from the origin. A shallower slope indicates a faster drop. For example, the fastest drop in R2A4 is faster than the fastest drop in R2A1, labeled by (A) and (B) in Fig. 13, respectively; a fact likewise confirmed by Fig. 7. Jets that break up with greater consistency or repeatability across trials create aggregated STDs with fewer lines or tracks, with each track having a higher intensity due to repeated superposition of individual jetting events. R3A1 and R3A6 channels, for example, break up more repeatably across trials than the other featured channels.

F. Spatiotemporal diagrams in y

Another convenient means of visualizing the trajectories of jets is an STD in the y -direction. STDs in y are created following the same approach as STDs in x , but the binary matrix in each frame is now summed along each row and reduced to a column vector. Column vectors are stacked in time to form the STD in y , which is a $k \times i$ matrix, where k is the number of y -pixels in the FOV and i is the number of frames. Aggregated STDs in y are shown for our featured channels in Fig. 14. The y origin runs along the nozzle centerline. Dimensional or breakup information of the jet is not obtained from the STD in y ; the plot instead gives the tendency to find a liquid parcel at a given y location in the FOV. Moreover, individual trajectories cannot be discerned, but net deviations can be visualized. Initially, when jets emerge from the nozzle, intensity values gradually increase as the liquid is drained from the channel and into the ligament. The intensity values reduce as the liquid parcels either exit the FOV or deviate from the centerline. The intensity reduction in the case of centerline deviation is also complemented by an increase in non-zero pixel rows in the column vector of each frame.

Individual plots are then aggregated by the same method as STDs in x . In the aggregated y - t STDs, focused and repeatable jets are those where the trajectories are narrow and have greater intensities as a result of superimposition. Such is the case when trailing drops follow the leading drop, and an overall jet trajectory can be distinguished. The STD can either be centered or skewed in one direction if there is a preferential jetting direction. In cases where there is a different motion of the tail with respect to the jet tip, there is a spread in the STDs in y .

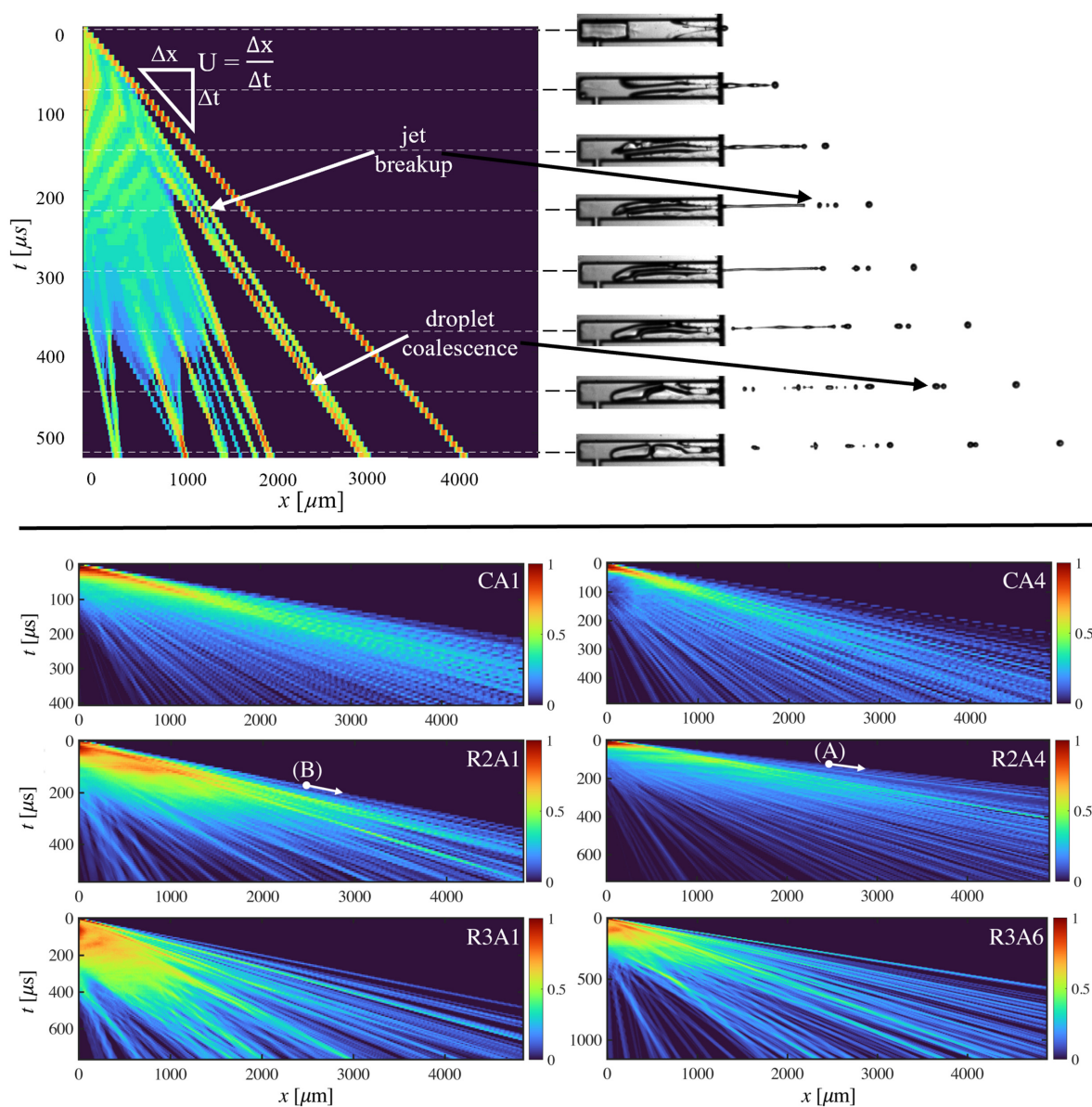


FIG. 13. Spatiotemporal diagrams (STDs) in x . Top: A spatiotemporal diagram for a single video with key attribute labels. Video snapshots correspond to times indicated in the STD. Bottom: Aggregated x - t STDs for featured channels. The number of trials N comprising each aggregate is given in Table II. Typically, $N = 20$. Labels (A) and (B) denote trajectories of the fastest leading drops.

In 14, the most repeatable jets are emitted from CA1 and R3A6. R2A1 has a large spread and, therefore, lower repeatability. The cause for the upward trajectory of jets produced by CA1 is unknown but again is likely the result of a slight upward tilt of the chip in its holder (approximately 0.5).

G. Focusing factor

Each column in Fig. 14, a snapshot in time, has a corresponding intensity curve across y . If time is collapsed and we take the maximum

intensity value at each y position, we render a single curve that represents the STD, as shown in Fig. 15. We may quantify the aggregate focus of a jet by the focusing factor F , defined as the full width at half maximum (FWHM) of the intensity curves in Fig. 15. Lower values of F correspond to more focused jets. We denote F , which has units of μm , as a red line in Fig. 15, and report F for all channels in Table II. The location of the peaks in the FWHM curves, and their skewness in one direction indicates a preferential jetting direction for the chip configuration (similar to the STDs in y); jets that emerge and travel at an angle from the chip, have peaks at an offset from 0, a trait that is

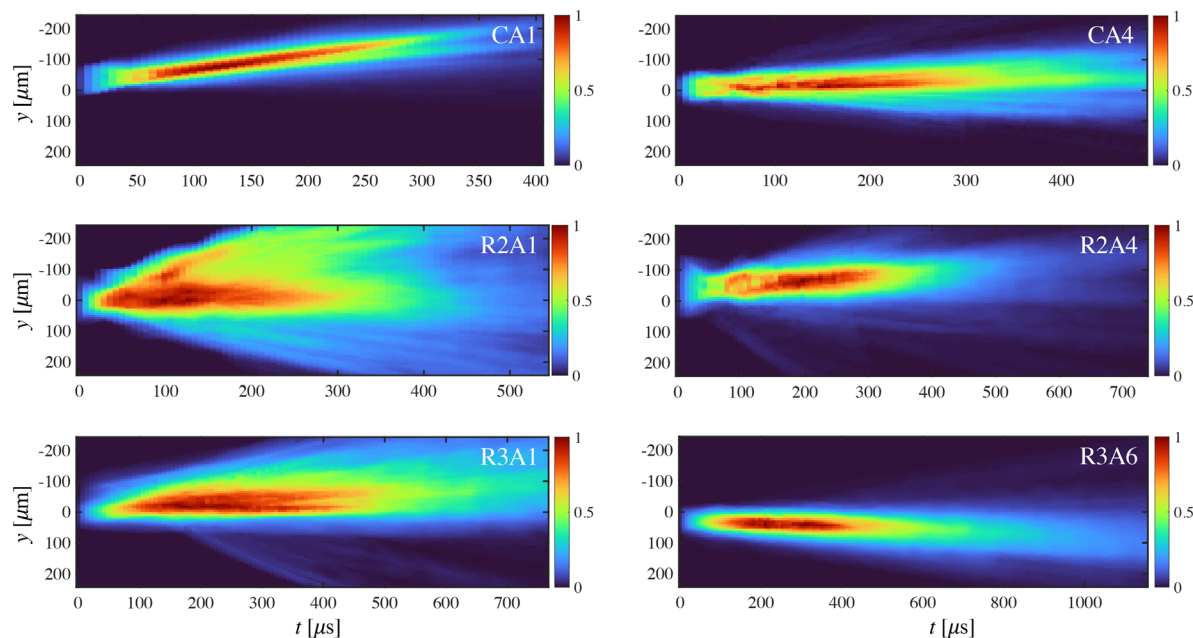


FIG. 14. Aggregated y - t spatiotemporal diagrams for featured channels are the foundation for the focusing factor. The number of trials N comprising each aggregate is given in Table II.

observed in almost all chips. A slight tilt in the positioning of the CA1 chip gives its jets an artificially high F . Otherwise, the shape of intensity curves and F values correspond well to the diffusive nature of jets shown in Fig. 14. All coated channels improve the focusing factor F over their uncoated (A1) counterparts, save R3A2. Overall, the most focused jets are produced by R3A4 and R3A6, indicating that the tallest channel (R3) inherently produces the most repeatable jets.

Since the effect of the bias in Fig. 11 is lost, we again turn to outline curves discussed above to make a comparison with the front-view trajectories. To be able to compare front and top views meaningfully, we focus on an area $1575 \times 482 \mu\text{m}$, $\approx 1/3$ rd of the FOV presented in Secs. III E and III F, located $2300 \mu\text{m}$ away from the chip edge (Fig. 16, top). The choice of this focus area is due to our inability to visualize the channel exit from the top. The corresponding outline curves are calculated with the same procedure as in Sec. III G and are presented in Fig. 16. Here, as in Sec. III G, the deviation of the peak from the center of these curves represents a bias in jetting direction. However, in contrast to curves in Fig. 15, the intensity values are not normalized. The intensity values correlate with the amount of fluid passing through the window, and therefore, the difference between these values allows us to compare the extent of out-of-axis behavior between both views.

We find that for the tall R3 channels, the jet body follows the directional bias (toward the top in the front view and toward the left in the top view) set by the jet tip in all cases (Fig. 16). For the asymmetric channels R3A2 and R3A6, the bias toward the z direction is marked by the location of the maximum values at $\approx -100 \mu\text{m}$ for both channels. The intensity curve derived from the top camera view is lowest for R3A6 among other R3 channels, indicating that most of the jet has left the FOV before entering this window. In contrast, the symmetric channels R3A4 and R3A8 have sharp distinct peaks near the center (deviation $< 50 \mu\text{m}$), with grayscale intensities > 200 , again supporting that symmetric coatings do not bias the jet trajectory. For

the lower aspect ratio R2 channels, we also find a bias of the jet body toward the z direction for both asymmetrically coated channels. For R2A2 channel, bias in z in the top view is denoted by the presence of a sharp peak at $\approx -80 \mu\text{m}$. For R2A6, this z bias is seen as well; the top outline curve looks similar to that of R3A6, following an extreme out-of-axis behavior. The maximum value of the front outline curves is at $y = 0$, with a wide distribution over y . This distribution is owed to plug flow in R2A6 instead of a focused jet tip, which makes the jet exit from the top or bottom of the channel.

For the circular channels, we find the bias toward the z direction expected for the asymmetrically coated CA2, and the centerline trajectory expected for the symmetrically coated CA4. The gradual decrease in intensities as we go from the circular and rectangular R2 to the rectangular R3 is owing to the greater tendency to form plug flows in the smaller channels, which is not so in the larger channels. The more complete emptying of the smaller channels due to the plug flow induced in the channel following the initial cavitation event gives rise to their greater intensity values.

IV. CONCLUDING REMARKS

In this experimental study, we present jet behaviors observed from micro-channels of three geometries with up to five coating configurations each. Channels are coated with alternating hydrophobic and hydrophilic bands along their periphery. Jets are generated by laser-induced thermocavitation and the channels are initially partially filled such that the advancing meniscus is kinematically focused. Modifications to the rapidly accelerated meniscus by the different coatings influence the jet breakup, the resulting drop size distribution, the trajectory of the jet tip, and the consistency of jet characteristics across trials. Our findings agree with previous studies that the jet velocity U has a linear relationship with the bubble growth velocity \dot{U}_{bub} , $U \sim \dot{U}_{\text{bub}}$, as shown in Fig. 7. No effect of the hydrophobic

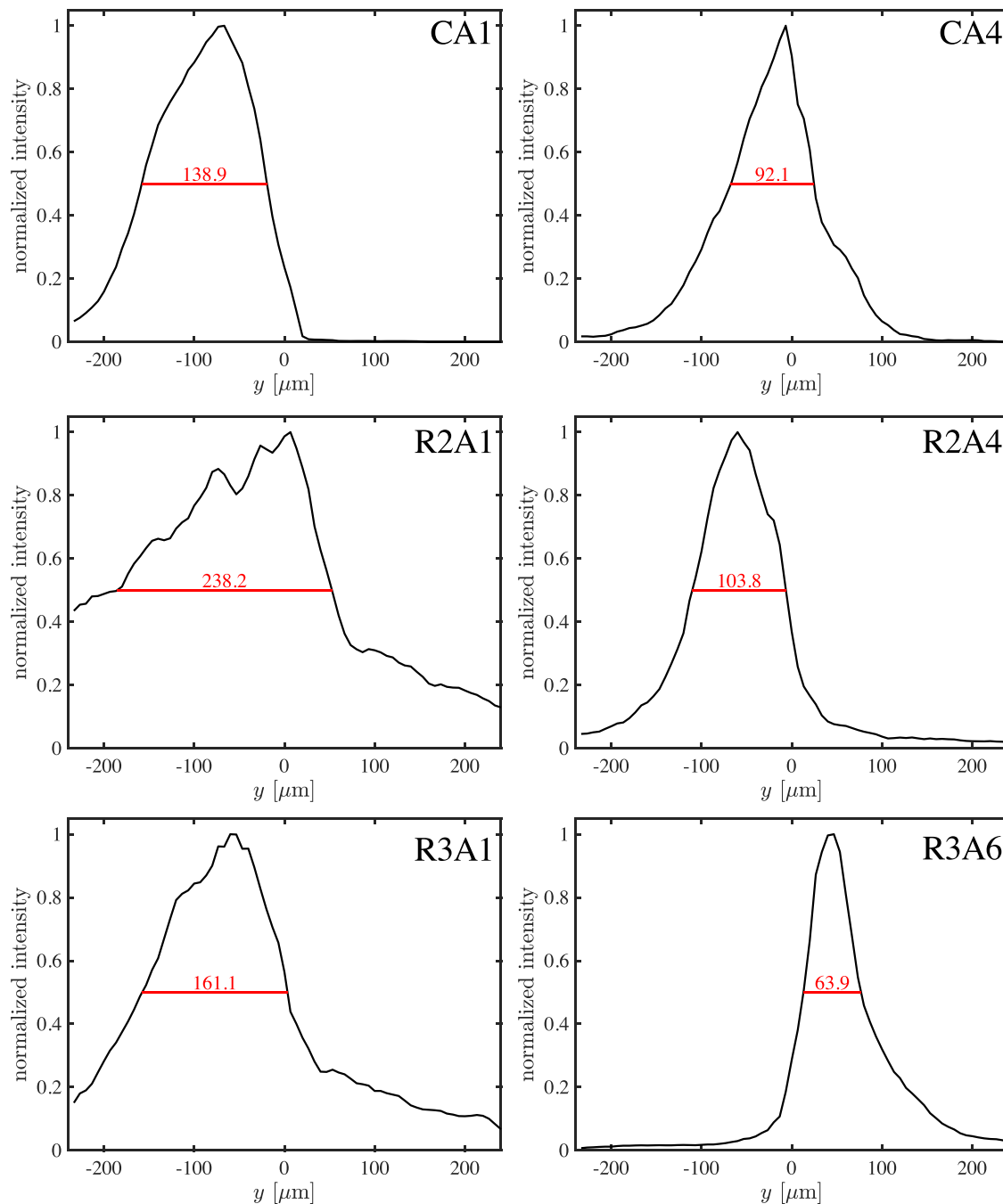


FIG. 15. Maximum normalized intensity derived from STDs in y , across jetting time t for all featured channels. Negative values indicate the top of the FOV (see Fig. 4). The red lines and values report the focusing factor F derived from the full width at half maximum of the normalized intensity curves.

coatings is observed for either the circular or the rectangular cross-sectioned R2 channels. In contrast, for the higher aspect ratio R3-coated channels, the ratio of jet to average bubble velocity U/\bar{U}_{bub} increases compared to the uncoated channels, indicating less hydrodynamic resistance to the rapid thermocavitation event.

We assessed how the coatings and their wettability influence the initial meniscus shape and contact line dynamics. These two factors are critical for understanding the jet tip direction and the jet body behavior. Asymmetrically coated channels produce an off-axis jet tip trajectory with a clear bias toward the hydrophobic channel wall.

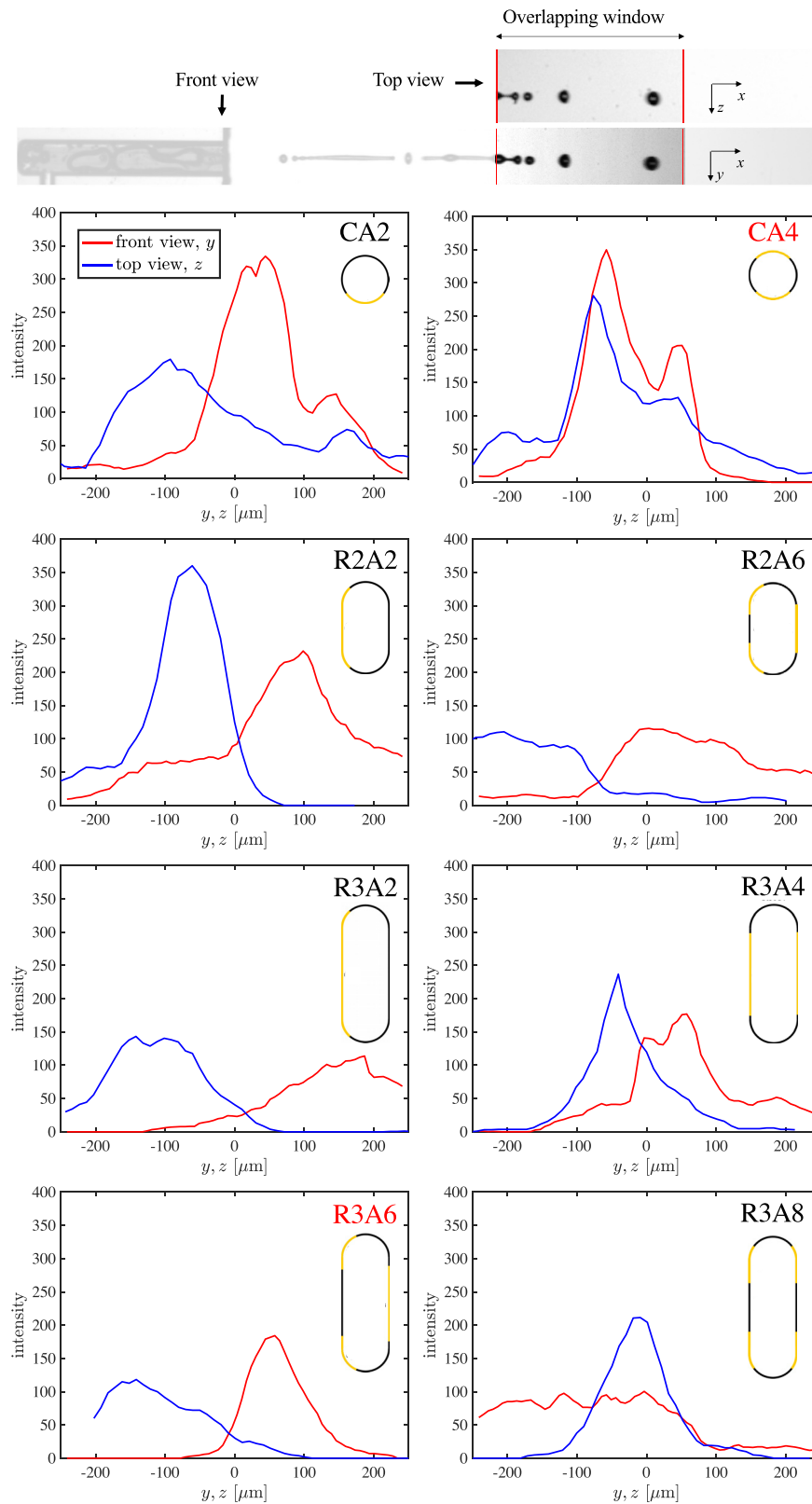


FIG. 16. Maximum intensity derived from partial-view STDs in y (red) and z (blue), across jetting time t . Negative values indicate the top of the FOV. Red channel labels indicate featured channels. Top panel: Diagram denoting the fields of analysis in both camera views for the partial-view STDs.

Although we could not image the meniscus from the top, we suggest that the asymmetrically shaped meniscus results in the observed flow focusing toward the hydrophobic wall. Furthermore, rectangular channels with a hydrophilic strip in the middle, such as R3A6, reduce the out-of-axis trajectory. This is due to the hydrophobic strips geometrically delimiting the flow of the jet in the middle of the channel. The effect of the energy barriers is reduced for circular channels and R2 channels due to their tendencies to produce plug-like jets; the emitted jets wet the whole perimeter of the channel and are wider than the hydrophilic strips, resulting in low flow focusing.

For the analysis of the jet dynamics in time and space, we have developed a spatiotemporal diagram (STD) representation, which can be generated in both the x and y directions. STDs in x give information about the jet breakup, coalescence, and the trajectory of individual drops. STDs in y give information about the asymmetric direction of the entire jet, tip, and body. By extracting the maximum intensity of each time in the y - t STDs, we can extract profiles that show concisely the jet bias off the centerline and the focusing factor F .

We avoid referring to any one channel as superior. The jetting characteristics from any particular channel may well be optimally suited to a particular application. For example, needle-free dermal injections will work best with jets that remain coherent over greater distances and exhibit limited off-axis behavior such as tail sway. Jets aimed at uniformly coating surfaces may work best with tails that deviate from the trajectory of their leading drops. We have studied the impact of microjets, from uncoated channels, on external substrates such as capillary bridges⁴⁷ and soft substrates.^{36,48} A logical next step in the research of coated channels is the characterization of deposition patterns these jets produce for a wide range of cavitation and channel parameters. The exquisite tunability of the present system through variation of geometry, heterogeneous surface chemistry, laser properties, and more pave a bright future for its adaption to a wide range of applications.

SUPPLEMENTARY MATERIAL

See the [supplementary material](#) for supplementary movie captions and a complete set of figures for each experimental channel.

ACKNOWLEDGMENTS

We would like to thank the National Science Foundation CBET-1941341 and the European Research Council (ERC) under the European Union Horizon 2020 Research and Innovation Program (Grant Agreement No. 851630) for support and McKenna E. M. Goss for text edits. Furthermore, we would like to thank Stefan Schlautmann for the fabrication of the microfluidic chips.

AUTHOR DECLARATIONS

Conflict of Interest

The authors have no conflicts to disclose.

Author Contributions

Jelle J. Schoppink and Keerthana Mohan contributed equally to this paper.

Jelle J. Schoppink: Data curation (lead); Formal analysis (lead); Investigation (lead); Methodology (equal); Validation (lead); Visualization

(lead); Writing – original draft (lead); Writing – review & editing (lead). **Keerthana Mohan:** Data curation (lead); Formal analysis (lead); Visualization (lead); Writing – original draft (lead); Writing – review & editing (lead). **Miguel Quetzeri-Santiago:** Data curation (equal); Formal analysis (equal); Investigation (equal); Visualization (equal); Writing – original draft (equal); Writing – review & editing (equal). **Gareth H. McKinley:** Writing – review & editing (equal). **David Fernandez Rivas:** Conceptualization (equal); Funding acquisition (supporting); Project administration (lead); Supervision (lead); Writing – review & editing (equal). **Andrew Keith Dickerson:** Conceptualization (equal); Data curation (equal); Formal analysis (lead); Funding acquisition (lead); Investigation (lead); Project administration (equal); Supervision (lead); Validation (equal); Visualization (lead); Writing – original draft (lead); Writing – review & editing (lead).

DATA AVAILABILITY

Raw data were generated at the OneDrive large scale facility. Derived data supporting the findings of this study are available from the corresponding author upon reasonable request.

REFERENCES

- ¹G. Bidone, *Expériences sur la forme et sur la direction des veines et des courants d'eau lancés par diverses ouvertures*, Par Georges Bidone (l'Imprimerie royale, 1829).
- ²F. Savart, "Memoire sur la constitution des veines liquides lancees par des orifices circulaires en mince paroi," *Anal. Chem.* **53**, 337–386 (1833).
- ³G. Amini, Y. Lv, A. Dolatabadi, and M. Ihme, "Instability of elliptic liquid jets: Temporal linear stability theory and experimental analysis," *Phys. Fluids* **26**, 114105 (2014).
- ⁴N. Ashgriz and A. Yarin, "Capillary instability of free liquid jets," in *Handbook of Atomization and Sprays* (Springer, 2011), pp. 3–53.
- ⁵J. Eggers and E. Villermaux, "Physics of liquid jets," *Rep. Prog. Phys.* **71**, 036601 (2008).
- ⁶W. Sirignano and C. Mehring, "Review of theory of distortion and disintegration of liquid streams," *Prog. Energy Combust. Sci.* **26**, 609–655 (2000).
- ⁷V. Entov and A. Yarin, "The dynamics of thin liquid jets in air," *J. Fluid Mech.* **140**, 91–111 (1984).
- ⁸V. Entov and A. Yarin, "Dynamical equations for a liquid jet," *Fluid Dyn.* **15**, 644–649 (1980).
- ⁹D. Jarrahbashi and W. A. Sirignano, "Acceleration effects on instability of high-pressure fuel jets," in *Proceedings of the Twelfth International Conference on Liquid Atomization and Spray Systems (ICLASS)* (ILASS International, 2012), pp. 1–8.
- ¹⁰S. Mitragotri, "Current status and future prospects of needle-free liquid jet injectors," *Nat. Rev. Drug Discovery* **5**, 543–548 (2006).
- ¹¹D. H. Reneker, A. L. Yarin, H. Fong, and S. Koombhongse, "Bending instability of electrically charged liquid jets of polymer solutions in electrospinning," *J. Appl. Phys.* **87**, 4531–4547 (2000).
- ¹²V. Menezes, S. Kumar, and K. Takayama, "Shock wave driven liquid microjets for drug delivery," *Phys. Fluids* **106**, 086102 (2009).
- ¹³Y. Tagawa, N. Oudalov, A. El Ghalbzouri, C. Sun, and D. Lohse, "Needle-free injection into skin and soft matter with highly focused microjets," *Lab Chip* **13**, 1357–1363 (2013).
- ¹⁴E. P. Furlani, B. G. Price, G. Hawkins, and A. G. Lopez, "Thermally induced marangoni instability of liquid microjets with application to continuous inkjet printing," in *Proceedings of NSTI Nanotechnology Conference* (Nano Science and Technology Institute, 2006), pp. 534–537.
- ¹⁵J. R. Castrejon-Pita, W. Baxter, J. Morgan, S. Temple, G. Martin, and I. M. Hutchings, "Future, opportunities and challenges of inkjet technologies," *Atomization Sprays* **23**, 541–565 (2013).
- ¹⁶J. C. Carter, R. M. Alvis, S. B. Brown, K. C. Langry, T. S. Wilson, M. T. McBride, M. Myrick, W. R. Cox, M. E. Grove, and B. W. Colston, "Fabricating

- optical fiber imaging sensors using inkjet printing technology: A pH sensor proof-of-concept," *Biosens. Bioelectron.* **21**, 1359–1364 (2006).
- ¹⁷D. MacFarlane, V. Narayan, J. Tatum, W. Cox, T. Chen, and D. Hayes, "Microjet fabrication of microlens arrays," *IEEE Photonics Technol. Lett.* **6**, 1112–1114 (1994).
 - ¹⁸A. Kiyama, Y. Tagawa, K. Ando, and M. Kameda, "Effects of a water hammer and cavitation on jet formation in a test tube," *J. Fluid Mech.* **787**, 224–236 (2016).
 - ¹⁹A. Antkowiak, N. Bremond, S. Le Dizes, and E. Villermaux, "Short-term dynamics of a density interface following an impact," *J. Fluid Mech.* **577**, 241–250 (2007).
 - ²⁰N. Reis, C. Ainsley, and B. Derby, "Ink-jet delivery of particle suspensions by piezoelectric droplet ejectors," *J. Appl. Phys.* **97**, 094903 (2005).
 - ²¹L. Oyarte Gálvez, A. Fraters, H. L. Offerhaus, M. Versluis, I. W. Hunter, and D. Fernández Rivas, "Microfluidics control the ballistic energy of thermocavitation liquid jets for needle-free injections," *J. Appl. Phys.* **127**, 104901 (2020).
 - ²²Y. Tagawa, N. Oudalov, C. W. Visser, I. R. Peters, D. van der Meer, C. Sun, A. Prosperetti, and D. Lohse, "Highly focused supersonic microjets," *Phys. Rev. X* **2**, 031002 (2012).
 - ²³I. R. Peters, Y. Tagawa, N. Oudalov, C. Sun, A. Prosperetti, D. Lohse, and D. van der Meer, "Highly focused supersonic microjets: Numerical simulations," *J. Fluid Mech.* **719**, 587–605 (2013).
 - ²⁴J. Schoppink and D. F. Rivas, "Jet injectors: Perspectives for small volume delivery with lasers," *Adv. Drug Delivery Rev.* **182**, 114109 (2022).
 - ²⁵J. Krizek, P. Delrot, and C. Moser, "Repetitive regime of highly focused liquid microjets for needle-free injection," *Sci. Rep.* **10**, 1–9 (2020).
 - ²⁶L. Rayleigh, "On the instability of jets," *Proc. London Math. Soc.* **1**, 4–13 (1878).
 - ²⁷*Handbook of Atomization and Sprays: Theory and Applications*, edited by N. Ashgriz (Springer Science & Business Media, 2011).
 - ²⁸C. B. Rodríguez, C. W. Visser, S. Schlautmann, D. F. Rivas, and R. Ramos-García, "Toward jet injection by continuous-wave laser cavitation," *J. Biomed. Opt.* **22**, 105003 (2017).
 - ²⁹J. M. Gordillo, H. Onuki, and Y. Tagawa, "Impulsive generation of jets by flow focusing," *J. Fluid Mech.* **894**, A3 (2020).
 - ³⁰A. M. Sterling and C. Sleicher, "The instability of capillary jets," *J. Fluid Mech.* **68**, 477–495 (1975).
 - ³¹M. Birouk and N. Lekic, "Liquid jet breakup in quiescent atmosphere: A review," *Atomization Sprays* **19**, 501–528 (2009).
 - ³²F. Wang and T. Fang, "Liquid jet breakup for non-circular orifices under low pressures," *Int. J. Multiphase Flow* **72**, 248–262 (2015).
 - ³³G. Amini and A. Dolatabadi, "Axis-switching and breakup of low-speed elliptic liquid jets," *Int. J. Multiphase Flow* **42**, 96–103 (2012).
 - ³⁴D. T. Jordan, N. M. Ribe, A. Deblais, and D. Bonn, "Chain oscillations in liquid jets," *Phys. Rev. Fluids* **7**, 104001 (2022).
 - ³⁵M. Park, H. Jang, F. V. Sirotkin, and J. J. Yoh, "Er:YAG laser pulse for small-dose splashback-free microjet transdermal drug delivery," *Opt. Lett.* **37**, 3894–3896 (2012).
 - ³⁶D. L. van der Ven, D. Morrone, M. A. Quetzeri-Santiago, and D. F. Rivas, "Microfluidic jet impact: Spreading, splashing, soft substrate deformation and injection," *J. Colloid Interface Sci.* **636**, 549 (2023).
 - ³⁷K. Cu, R. Bansal, S. Mitragotri, and D. Fernandez Rivas, "Delivery strategies for skin: Comparison of nanoliter jets, needles and topical solutions," *Ann. Biomed. Eng.* **48**, 2028–2039 (2020).
 - ³⁸H. Notsu, W. Kubo, I. Shitanda, and T. Tatsuma, "Super-hydrophobic/super-hydrophilic patterning of gold surfaces by photocatalytic lithography," *J. Mater. Chem.* **15**, 1523–1527 (2005).
 - ³⁹R. Deng, Y. He, Y. Qin, Q. Chen, and L. Chen, "Measuring pure water absorption coefficient in the near-infrared spectrum (900–2500 nm)," *J. Remote Sens.* **16**, 192–206 (2012).
 - ⁴⁰M. A. Quetzeri-Santiago, I. W. Hunter, D. Van Der Meer, and D. F. Rivas, "Impact of a microfluidic jet on a pendant droplet," *Soft Matter* **17**, 7466–7475 (2021).
 - ⁴¹B. Zhang, D. Banks, V. Robles, L. F. Devia Cruz, and G. Aguilar, "High resolution optical investigation of laser intensity and solution temperature effects on thermocavitation," *Exp. Therm. Fluid Sci.* **136**, 110683 (2022).
 - ⁴²C. Clanet and J. Lasheras, "Transition from dripping to jetting," *J. Fluid Mech.* **383**, 307–326 (1999).
 - ⁴³P. Marmottant and E. Villermaux, "Fragmentation of stretched liquid ligaments," *Phys. Fluids* **16**, 2732–2741 (2004).
 - ⁴⁴B. Keshavarz, E. C. Houze, J. R. Moore, M. R. Koerner, and G. H. McKinley, "Ligament mediated fragmentation of viscoelastic liquids," *Phys. Rev. Lett.* **117**, 154502 (2016).
 - ⁴⁵S. Kooij, R. Sijs, M. M. Denn, E. Villermaux, and D. Bonn, "What determines the drop size in sprays?," *Phys. Rev. X* **8**, 031019 (2018).
 - ⁴⁶E. Villermaux, "Fragmentation versus cohesion," *J. Fluid Mech.* **898**, P1 (2020).
 - ⁴⁷M. A. Quetzeri-Santiago and D. F. Rivas, "Cavity dynamics after the injection of a microfluidic jet onto capillary bridges," *Soft Matter* **19**, 245–257 (2023).
 - ⁴⁸L. Oyarte Gálvez, M. Brió Pérez, and D. Fernández Rivas, "High speed imaging of solid needle and liquid micro-jet injections," *J. Appl. Phys.* **125**, 144504 (2019).